The Astrophysical Journal Letters, 954:L43 (9pp), 2023 September 10 https://doi.org/10.3847/2041-8213/ace32b

A Dynamically Distinct Stellar Population in the Leading Arm of the Sagittarius Stream

Gwibong Kang[1], Young Sun Lee[2,3], Young Kwang Kim[2], and Timothy C. Beers[3]
[1] Department of Astronomy, Space Science, and Geology, Chungnam National University, Daejeon 34134, Republic of Korea
[2] Department of Astronomy and Space Science, Chungnam National University, Daejeon 34134, Republic of Korea; youngsun@cnu.ac.kr
[3] Department of Physics and Astronomy and JINA Center for the Evolution of the Elements, University of Notre Dame, IN 46556, USA
Received 2023 March 29; revised 2023 June 6; accepted 2023 June 26; published 2023 September 11

Abstract

We present a chemical and dynamical analysis of the leading arm (LA) and trailing arm (TA) of the Sagittarius (Sgr) stream, as well as for the Sgr dwarf galaxy core (SC), using red giant branch, main-sequence, and RR Lyrae stars from large spectroscopic survey data. The different chemical properties among the LA, TA, and SC generally agree with recent studies and can be understood by a radial metallicity gradient established in the progenitor of the Sgr dwarf, followed by preferential stellar stripping from the outer part of the Sgr progenitor. One striking finding is a relatively larger fraction of low-eccentricity stars ($e < 0.4$) in the LA than in the TA and SC. The TA and SC exhibit very similar distributions. Considering that a tidal tail stripped off from a dwarf galaxy maintains the orbital properties of its progenitor, we expect that the *e*-distribution of the LA should be similar to that of the TA and SC. Thus, the disparate behavior of the *e*-distribution of the LA is of particular interest. Following the analysis of Vasiliev et al., we attempt to explain the different *e*-distribution by introducing a time-dependent perturbation of the Milky Way by the Large Magellanic Cloud's (LMC) gravitational pull, resulting in substantial evolution of the angular momentum of the LA stars to produce the low-*e* stars. In addition, we confirm from RR Lyrae stars with high eccentricity ($e > 0.6$) that the TA stars farther away from the SC are also affected by disturbances from the LMC.

Unified Astronomy Thesaurus concepts: Milky Way dynamics (1051); Sagittarius dwarf spheroidal galaxy (1423); Stellar streams (2166); Dwarf galaxies (416); Stellar dynamics (1596); Stellar abundances (1577)

1. Introduction

Numerous studies have argued that some or all of the halo system of the Milky Way (MW) has formed through multiple mergers with dwarf galaxies of various masses (e.g., Bullock & Johnston 2005; Cooper et al. 2010), likely over an extended period of time. An excellent example of one such merging episode is the Sagittarius (Sgr) dwarf spheroidal galaxy, which is in the process of being tidally disrupted (Ibata et al. 1994). The Sgr dwarf was discovered as an overdensity of stars with distinctive velocities and positions in the sky (Ibata et al. 1994; Majewski et al. 2003; Belokurov et al. 2006). Subsequently, the Sgr tidal stream was discovered (Yanny et al. 2000; Ibata et al. 2001), and its detailed shape was later confirmed (Newberg et al. 2002; Majewski et al. 2003). The Sgr stellar stream appears to wrap around the MW two or three times (e.g., Majewski et al. 2003; Law & Majewski 2010; Belokurov et al. 2014) and consists of two arms, the leading arm (LA) and trailing arm (TA).

Recent studies have identified a significant metallicity discrepancy between the LA and TA, with the former being more metal-poor by about 0.3 dex (Carlin et al. 2018; Li et al. 2019; Hayes et al. 2020; Ramos et al. 2022). In addition, a metallicity gradient has been detected not only in the Sgr core (SC) but also in the Sgr stream (Carlin et al. 2012; Gibbons et al. 2017; Hayes et al. 2020; Ramos et al. 2022). These chemical patterns imply the existence of a significant metallicity gradient in the Sgr progenitor galaxy. The observed metallicity difference between the two arms and the core is thought to be the result of the selective stripping of older, more metal-poor stars located in the outermost regions of the Sgr progenitor. It has also been reported that, within each arm, the metal-poor stars exhibit larger velocity dispersions than the relatively more metal-rich stars (Gibbons et al. 2017; Johnson et al. 2020; Limberg et al. 2023).

This overall picture has become even more complicated with the discovery of bifurcation in each arm (Belokurov et al. 2006; Koposov et al. 2012), requiring a more detailed analysis of each arm. In addition, Vasiliev et al. (2021, hereafter V21) reported a misalignment between the Sgr stream track and the motion of the LA stars (corrected for the solar reflex motion in their observed proper motions). They explained such a misalignment by introducing the time-dependent perturbation of the MW caused by the Large Magellanic Cloud (LMC). Their finding demonstrated that the role of the LMC should be taken into account for a better understanding of the dynamical properties and evolution of the Sgr stream.

In this letter, we employ red giant branch (RGB), main-sequence (MS), and RR Lyrae stars to identify the presence of a large fraction of low-eccentricity ($e < 0.4$) stars in the LA, as compared to both the TA and the SC, which we take as a telltale sign of the dynamical evolution of the LA due to time-dependent perturbations.

Section 2 describes the spectroscopic survey data from which members of the Sgr stream and core are obtained, along with calculations of their orbital parameters. Section 3 outlines how we select the genuine Sgr member stars. In Section 4, we present the abundance and dynamical characteristics of the Sgr members and discuss the possible origins of low-eccentricity stars in the LA. Our conclusions are presented in Section 5.

2. Initial Samples

2.1. Large Spectroscopic Survey Data

To gather large numbers of stars useful for the selection of members in the SC and stream, we combined various large spectroscopic survey data from the Sloan Digital Sky Survey (SDSS; York et al. 2000) and its various subsurveys, in particular the Sloan Extension for Galactic Understanding and Exploration (SEGUE; Yanny et al. 2009; Rockosi et al. 2022) and the Apache Point Observatory Galactic Evolution Experiment Data Release 17 (APOGEE DR17; Abdurro'uf et al. 2022), as well as the Large sky Area Multi-Object Fiber Spectroscopic Telescope Data Release 5 (LAMOST DR5; Luo et al. 2019). We obtained stellar parameters such as effective temperature ($T_{\rm eff}$), surface gravity ($\log g$), and metallicity ([Fe/H]) by processing the SDSS and LAMOST spectra with signal-to-noise ratios (S/Ns) larger than 10 through the SEGUE Stellar Parameter Pipeline (SSPP; Lee et al. 2008a, 2008b, 2011). The interested reader is referred to Lee et al. (2015) for the application of the SSPP on the LAMOST spectra. Note that the SSPP also produces estimates of [Mg/Fe] for both of the lower-resolution spectroscopic surveys. In order to ensure reliable chemical abundance ratios of APOGEE stars, which were derived from the APOGEE Stellar Parameters and Chemical Abundances Pipeline (ASPCAP; García Pérez et al. 2016), we only selected stars with S/N $>$ 50 and $\log g < 4.3$ from APOGEE DR17.

As reported by Lee et al. (2023), the stellar parameters and abundances for the SDSS and LAMOST stars agree very well; the mean difference is about 0.1 dex for [Fe/H] and 0.01 dex for [Mg/Fe]. Similarly, we found a mean offset of –0.04 dex for [Fe/H] and –0.02 dex for [Mg/Fe] using stars in common between SDSS/LAMOST and APOGEE. Because the systematic offsets between surveys are less than the typical uncertainties (∼0.2 dex for [Fe/H] and ∼0.1 dex for [Mg/Fe]), we did not adjust for the small mean offsets. We placed the radial velocity (RV) of the SDSS/LAMOST stars on the scale of the RVs reported in the Gaia Early Data Release (EDR3; Gaia Collaboration et al. 2021) using the stars in common, as described in Lee et al. (2023).

The distance estimates for the SDSS stars were obtained by employing the method of Beers et al. (2000, 2012); the reported uncertainty is on the order of 15%–20%, while that of the LAMOST stars was taken from the value-added catalog of LAMOST DR5 (Xiang et al. 2019). The distances in this catalog were estimated based on a Bayesian approach (Wang et al. 2016); its uncertainty is about 20%. We employed the AstroNN spectrophotometric distance obtained from a deep neural network approach for the APOGEE stars (Leung & Bovy 2019). The quoted uncertainty is less than 10%.

In this study, we selected bright RGB and MS stars, which can probe up to the distance of the SC and stream by imposing the following cuts: $0.3 \leqslant (g-r) \leqslant 1.2$, $\log g < 3.5$, and $4400\,{\rm K} \leqslant T_{\rm eff} \leqslant 5600\,{\rm K}$ for the RGB stars. For the MS stars, cuts of $0.0 \leqslant (g-r) \leqslant 1.2$, $\log g \geqslant 3.5$, and $4400\,{\rm K} \leqslant T_{\rm eff} \leqslant 7000\,{\rm K}$ were adopted.

Note that we have removed stars located in or near known globular and open clusters. For multiply observed stars, we chose to include the star with the highest S/N or the one observed in APOGEE if a star was observed in both APOGEE and SDSS/LAMOST. Upon applying these various cuts, we obtained a total of approximately 2.9 million stars from SDSS/LAMOST and about 630,000 stars from APOGEE.

2.2. Space Velocity and Orbital Parameters

In order to calculate the orbital parameters of our program stars, we employed a Stäckel-type potential used by numerous previous studies (Kim et al. 2019, 2021, 2023; Lee et al. 2019, 2023; Chiba & Beers 2000). We adopted a local standard of rest velocity ($V_{\rm LSR}$) = 236 km s^{-1} (Kawata et al. 2019), a solar position of $R_\odot$ = 8.2 kpc (Bland-Hawthorn & Gerhard 2016), $Z_\odot$ = 20.8 pc (Bennett & Bovy 2019), and a solar peculiar motion of $(U, V, W)_\odot$ = (–11.10, 12.24, 7.25) km s^{-1} (Schönrich et al. 2010). We also computed the maximum ($r_{\rm max}$) and minimum ($r_{\rm min}$) distances from the Galactic center, orbital eccentricity (e) defined by $(r_{\rm max} - r_{\rm min})/(r_{\rm max} + r_{\rm min})$, angular momentum ($L$), and energy ($E$) for each star. The Galactic standard RV ($V_{\rm GSR}$) was calculated by $V_{\rm GSR} = V_{\rm H} - U_\odot \cos(l)\cos(b) + (V_{\rm LSR} + V_\odot)\sin(l)\cos(b) + W_\odot \sin(b)$, where $V_{\rm H}$ is the heliocentric RV. The uncertainty of each computed quantity was estimated by incorporating the errors in the distance, proper motion, and RV for each star.

We repeated the same calculations for the simulated Sgr stars under the influence of the MW interacting with the LMC using the coordinates, distances, proper motions, and RVs provided by V21.[4] We use our calculated eccentricity, angular momentum, and energy for these model stars to compare with our Sgr member stars from the RGB/MS and RR Lyrae samples, as described in Section 4.

3. Selection of Sgr Stellar Stream Stars

3.1. The RGB and MS Samples

The success of this study depends on how well we identify genuine members of the Sgr stellar stream. Because identifying stellar debris in a coordinate system aligned with a stellar stream can improve its characterization (Majewski et al. 2003; Belokurov et al. 2014), we introduced the Sgr stream coordinates (Λ, B) to select the members of the Sgr stream and converted the equatorial coordinates (α, δ) to Sgr stream coordinates using the prescription of Belokurov et al. (2014). In these coordinates, the Sgr longitude (Λ) increases in the direction of the SC motion, and the Sgr latitude (B) points to the north Galactic pole. We made use of the positional and kinematic information with respect to the Sgr orbital plane and devised the following two-step selection criteria based on the Sgr members provided by V21 to reduce contamination.

1. Based on the spatial distribution and distances of the Sgr stream stars, we initially select stars that are within $-20^\circ < B < 15^\circ$ and located at a heliocentric distance larger than d = 12 kpc (Belokurov et al. 2014; Ibata et al. 2020). Then, we apply a broad kinematic cut of $L_{\rm Y} < -0.3L_{\rm Z} - 2.5 \times 10^3$ kpc km s^{-1} (Li et al. 2019; Jönsson et al. 2020; Naidu et al. 2020). The gray dots in Figure 1 indicate the stars that pass these initial cuts. These stars exhibit a broad scatter in all four panels, indicating that they are not completely free of contamination from non-Sgr stars.
2. In the second step, we employ the Sgr member catalog provided by V21 to further reduce the halo interlopers.

[4] Model data can be downloaded from https://zenodo.org/record/4038141.

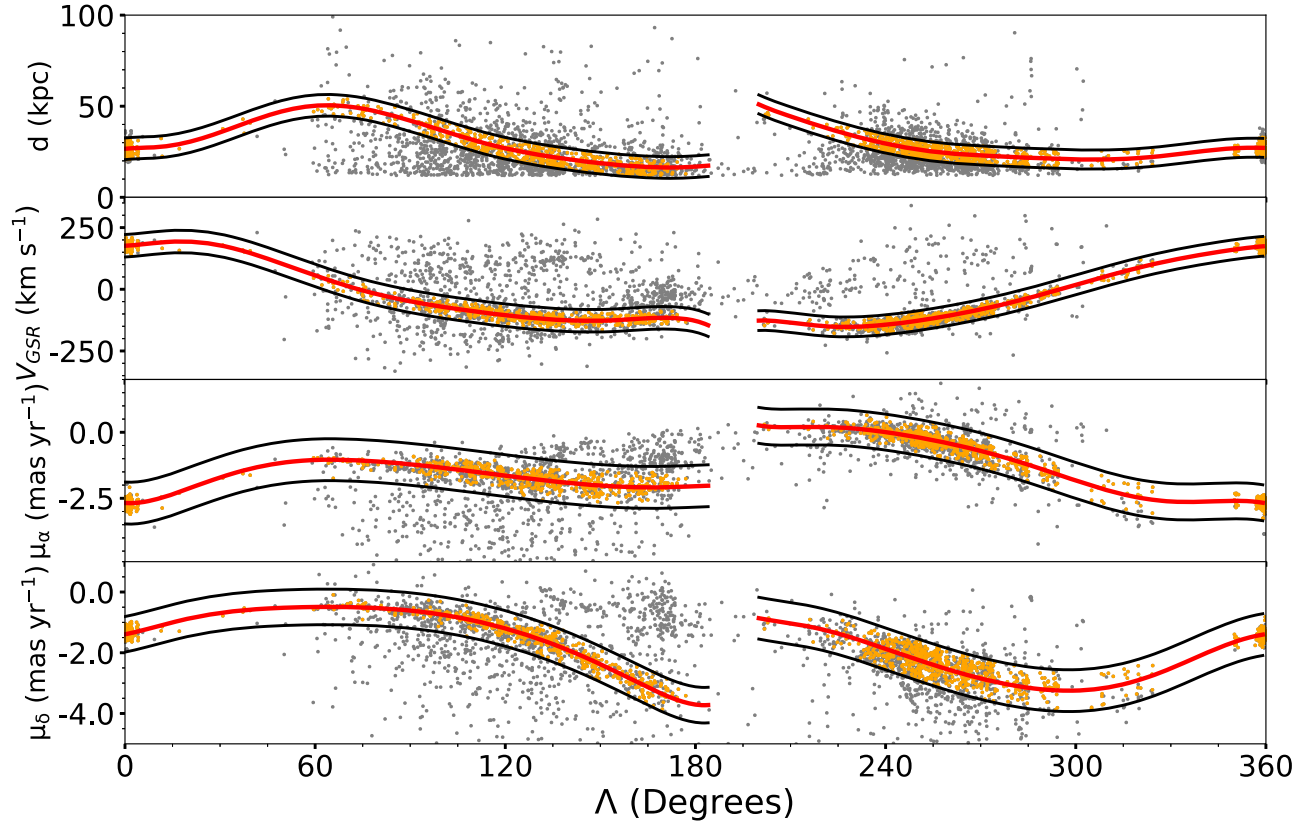

Figure 1. Distribution of heliocentric distance (d), $V_{\rm GSR}$, μ_α, and μ_δ of the Sgr candidates as a function of the Sgr stream longitude (Λ). The gray dots represent the stars in $-20^\circ < B < 15^\circ$, where B is the Sgr stream latitude, $d > 12$ kpc, and $L_Y < -0.3L_Z - 2.5 \times 10^3$ kpc km s^{-1}. The red line in each panel is the fiducial used to select the likely Sgr member stars, derived by a polynomial fit to the Sgr members in the catalog provided by V21. The black line delineates the $\pm 3\sigma$ curve from the fiducial, except for the distance panel, considering the photometric distance error, which is set to $\pm 4\sigma$ from the fiducial. The orange dots indicate the stars within the black curves in all four panels. The cluster around $\Lambda = 0^\circ$ and 360° is the SC. The stars with $\Lambda < 180^\circ$ belong to the LA, while the ones with $\Lambda > 200^\circ$ belong to the TA.

The catalog includes 55,192 Sgr stars selected based on $|B| < 10^\circ$. To enhance the reliability of our Sgr selection, we acquire proper-motion values of the catalog by matching with Gaia EDR3. We then consider the distribution of the Sgr candidates in four parameter spaces (distance, $V_{\rm GSR}$, μ_α, and μ_δ) as a function of the stream longitude (Λ), as shown in Figure 1. We then carry out a polynomial fit in each parameter to obtain a fiducial line as a function of Λ. Each fiducial is indicated with a red line in Figure 1. The black lines in Figure 1 are located $\pm 3\sigma$ from the fiducial line, except for the distance, which is $\pm 4\sigma$ from the fiducial line, considering the relatively large error of the photometric-based distance estimates of our program stars. To ensure that genuine Sgr member stars are chosen, we select objects that reside within the black curves in the four regions. These stars are our final Sgr stream and SC samples, marked in orange in Figure 1. The stars with $\Lambda < 180^\circ$ belong to the LA, while the ones with $\Lambda > 200^\circ$ belong to the TA.

Following the above selection procedure, we identified 2380 RGB stars (1369 from APOGEE; 817 from SDSS, primarily SEGUE; and 194 from LAMOST) and 37 MS stars, which come only from SDSS, resulting in a total of 2417 RGB/MS stars identified as likely Sgr members. Among them, the LA comprises 555 RGB and 23 MS stars, with 662 RGB and 14 MS stars for the TA. We have only RGB stars available from APOGEE for the SC. Consequently, the impact of the MS stars on our analysis and interpretation is very minimal, even if there are any systematics in chemical abundances and orbital parameters between the RGB and MS stars.

Because the Sgr stars are mostly located in the distant halo, we further checked the distance uncertainty for the selected Sgr members after separating them into different luminosity classes and survey data. By comparing the stars in common between SDSS and Gaia EDR3, we obtained relative uncertainties of $22\% \pm 1\%$ and $20\% \pm 1\%$ for the SDSS RGB and MS stars, respectively. During this process, we adjusted for the reported zero-point offset of –0.017 mas in Gaia EDR3 (Lindegren et al. 2021) and considered only the stars with relative parallax errors smaller than 10%. We estimated the distance uncertainties for the APOGEE and LAMOST RGB stars by taking a median value from the distribution of their quoted errors in their catalog. They are $27\% \pm 5\%$ and $22\% \pm 8\%$ for the APOGEE and LAMOST RGB stars, respectively.

3.2. The RR Lyrae Sample

Among the fundamental difficulties in the study of the Sgr stream is its large distance from the Sun ($\geqslant$10 kpc) and an uncertain kinematic analysis due to the small number of stars close to the SC, along with distance errors that become increasingly larger with increasing distance from the Sun. This challenge can be partially rectified by using old stellar populations of similar luminosity, such as blue horizontal

branch and RR Lyrae stars (e.g., Belokurov et al. 2014; Hernitschek et al. 2017; Ramos et al. 2020). Hence, to increase the reliability of the dynamical analysis of our RGB/MS Sgr member stars, we introduced a large number of RR Lyrae stars assembled by Ramos et al. (2020), which have more accurate distance estimates, and carried out their dynamical analysis as well. This sample includes about 11,700 RR Lyrae stars in the Sgr stream and core, selected based on the positions, distances, and proper motions from PanSTARRS1 (Chambers et al. 2016) and Gaia DR2 (Hernitschek et al. 2017). We gathered ∼7900 RR Lyrae stars that meet the selection criteria outlined in Section 3.1. See below how we obtained their RVs and orbital parameters.

One shortcoming of this sample is the lack of the RV information, which is indispensable to derive the orbital parameters. In order to overcome this deficiency and retrieve the RV information, we have devised the following procedure using a Monte Carlo (MC) simulation.

If the selected RR Lyrae stars are indeed members of the Sgr stream and/or core, their $V_{\rm GSR}$ values should fall inside the range indicated by the black lines in Figure 1. On that basis, we attempted to recover the RV information using the $V_{\rm GSR}$ fitting line and σ values derived in Figure 1. To check the reliability of this approach, we first tested this procedure with the 2417 Sgr member stars of the RGB/MS sample that we obtained in Section 3.1. To begin, we assumed that there was no RV for this sample of stars and hence no $V_{\rm GSR}$ value. Then we employed the fiducial line (red line) of $V_{\rm GSR}$ and σ as estimates of the mean and standard deviation of the $V_{\rm GSR}$ at a given Λ, obtained in the second panel of Figure 1. Then, by assuming a Gaussian error distribution for $V_{\rm GSR}$, we randomly drew a $V_{\rm GSR}$ value and assigned it to each star at a specific Λ. We repeated this process 1000 times to create 1000 simulated values of $V_{\rm GSR}$ for each object. Finally, we calculated a mean value of $V_{\rm GSR}$ and plugged it into the $V_{\rm GSR}$ equation used in Section 2 to retrieve the RV value required to calculate the orbital parameters, including the eccentricity.

A comparison of the retrieved RV obtained by the above method with the observed RV for our RGB/MS stars yielded a mean offset of 0.4 km s^{-1} with a standard deviation of 19.0 km s^{-1}, indicating that the retrieved RV from the MC simulation remains within 2σ of the quoted error value (∼10 km s^{-1}). In addition, a comparison of the derived eccentricity revealed a mean difference of only $\Delta(e) = 0.02$ with a standard deviation of $\sigma(e) = 0.04$. This exercise confirms the robustness of our approach to recover the RV information for the RR Lyrae stars. We applied the same method to the selected Sgr members of RR Lyrae stars to assign the RV and calculated their eccentricity, angular momentum, and energy.

4. Results and Discussion

4.1. Chemical Properties

Panel (a) of Figure 2 exhibits the metallicity distribution function (MDF) of our Sgr stream and SC members of our RGB/MS sample, while panel (b) is for the [Mg/Fe] distribution. The LA, TA, and SC members are represented by blue, red, and green, respectively. The MDFs indicate that the LA and TA have a broad distribution, with the former being overall more metal-poor than the latter, while the SC is dominated by more metal-rich stars with a narrow peak. The mean metallicity of the LA is $\langle[{\rm Fe/H}]_{\rm LA}\rangle = -1.14 \pm 0.12$ (sys) $\pm$ 0.03 (ran), where the systematic error (sys) was derived by the standard deviation of the median metallicities of APOGEE RGB, SDSS RGB, LAMOST RGB, and SDSS MS stars in the LA. The random uncertainty (ran) was computed by error propagation of the available random errors of the four subsamples. Similarly, the mean metallicities of the TA and SC are $\langle[{\rm Fe/H}]_{\rm TA}\rangle = -0.92 \pm 0.07$ (sys) $\pm$ 0.03 (ran) and $\langle[{\rm Fe/H}]_{\rm SC}\rangle = -0.56 \pm 0.01$ (ran), respectively. Note that as we have only the giant stars from APOGEE in the SC, we did not estimate the systematic error. Our derived mean values agree well with recent studies (e.g., Hayes et al. 2020; Ramos et al. 2022; Limberg et al. 2023).

Panel (c) of Figure 2 shows the MDFs of the TA and LA for the RR Lyrae stars. Although the peaks of the MDFs for the LA and TA occur at relatively lower metallicity (around [Fe/H] = –1.68 and –1.50, respectively) than the RGB/MS sample, due to the nature of their old stellar population, we clearly notice the systematic difference in the MDFs between the LA and TA.

Panel (b) of Figure 2 reveals that, while the SC has a narrow symmetric distribution of [Mg/Fe], the distribution of the LA and TA is skewed to higher [Mg/Fe]. Quantitatively, we obtained mean [Mg/Fe] values of $+0.08 \pm 0.07$ (sys) $\pm$ 0.07 (ran), $+0.08 \pm 0.07$ (sys) $\pm$ 0.06 (ran), and -0.05 ± 0.02 (ran) for the LA, TA, and SC, respectively. The systematic and random errors were calculated in the same way as for [Fe/H]. Hayes et al. (2020) found that the median [Mg/Fe] ratios of the LA, TA, and SC are +0.03, –0.01, and –0.03, respectively, while Ramos et al. (2022) obtained a mean value of [α/Fe] = +0.07 and +0.04 for the LA and TA, respectively. These estimates are in good agreement with ours within the errors.

The chemical contrasts between the LA, TA, and SC suggest that the Sgr progenitor had a different star formation history in its center and outskirts, with a higher rate of star formation in its center and a lower rate in its outskirts, establishing a radial abundance gradient. According to the *N*-body simulation of the Sgr tidal disruption by Law & Majewski (2010), the TA stars were stripped within the past ∼0.7–3.0 Gyr, while the LA stars were stripped ∼2.7–5.0 Gyr ago. Due to the outside-in nature of tidal stripping acting on a Sgr progenitor with abundance gradients (e.g., Law & Majewski 2010; Carlin et al. 2018; Hayes et al. 2020), the stars in the LA, which were stripped first, are more metal-poor than the ones in the TA. The higher [Mg/Fe] implies that the stars in the Sgr stream formed more rapidly, likely over a shorter timescale and with a higher rate of star formation (Hayes et al. 2020). In line with this, Hayes et al. (2020) found that their dynamically younger TA sample falls between the LA and SC in both the [Fe/H] and α-element abundances, suggesting that both gradients were first established in the Sgr progenitor.

4.2. Dynamical Properties

Panel (d) of Figure 2 shows the eccentricity (e) distribution of the LA (blue), TA (red), and SC (green) for our RGB/MS sample. One striking feature is that, although there is an overlapping region, the e-distribution of the LA is completely different from that of the TA and SC. The TA and SC exhibit very similar distributions to each other, biased toward higher eccentricity ($e > 0.4$). We found median eccentricities of 0.34 ± 0.06, 0.55 ± 0.05, and 0.52 ± 0.08 for the LA, TA, and SC, respectively. Separating into the RGB and MS

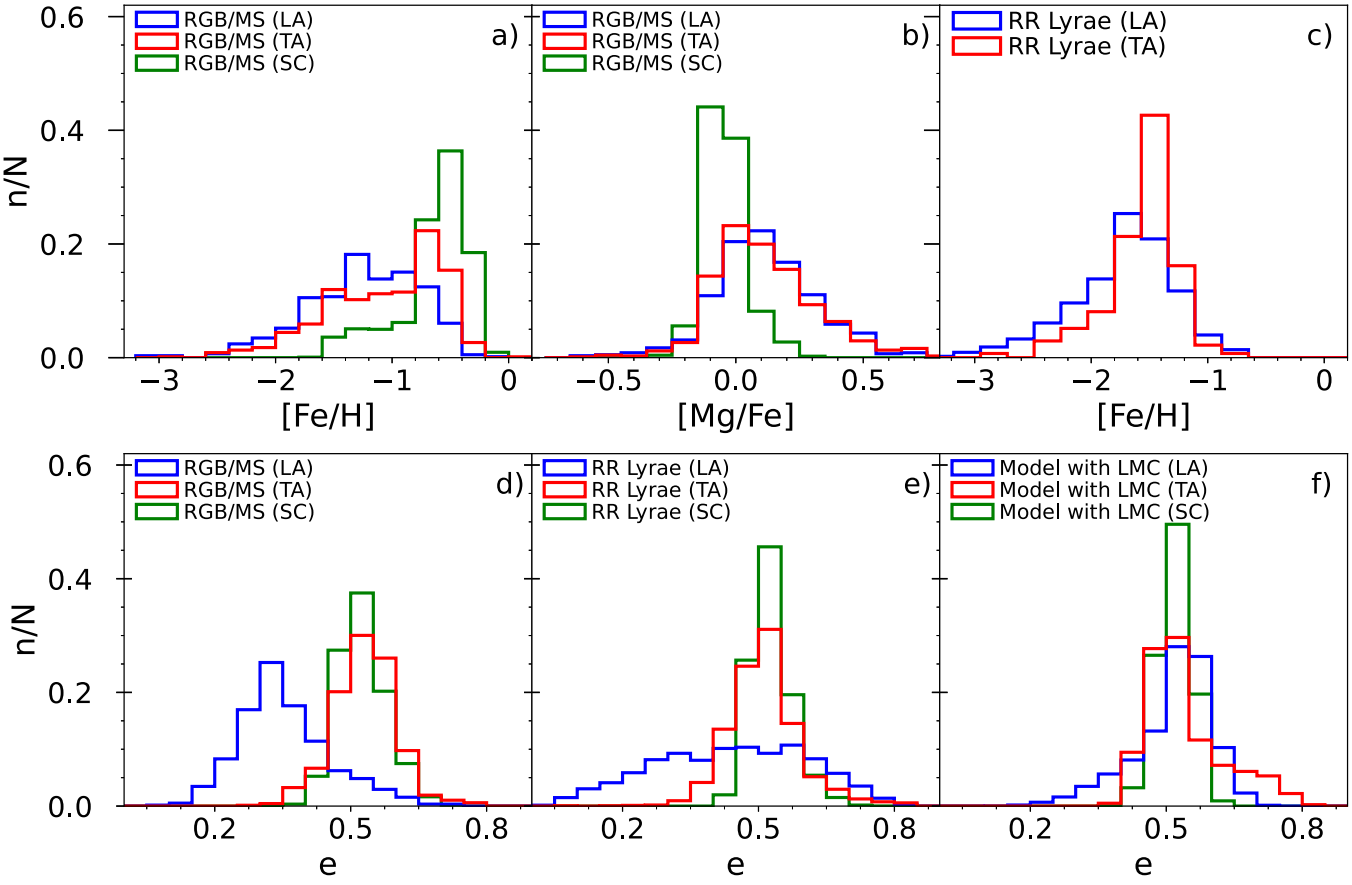

Figure 2. Top panels: distribution of [Fe/H] (left) and [Mg/Fe] (middle) for RGB/MS stars and [Fe/H] (right) for RR Lyrae stars. The metallicity information for the RR Lyrae stars was obtained by cross-matching the RR Lyrae catalog of Ramos et al. (2020) with SDSS/LAMOST data. The blue, red, and green histograms in each panel indicate the LA, TA, and SC, respectively. Each histogram is normalized by the total number of stars in each category. Note that there are no [Mg/Fe] distributions for the RR Lyrae stars and no SC histogram in the right panel because there are no SC stars in the SDSS/LAMOST data. Bottom panels: same as the top panels but for the distribution of eccentricity for the RGB/MS (left), RR Lyrae (middle), and simulated Sgr stars with the LMC (right) from V21. We note the large fraction of low-e stars in the LA, and a similar behavior is observed in the model as well.

subsamples yielded 0.34 ± 0.06 for the RGB and 0.33 ± 0.08 for the MS in the LA and 0.53 ± 0.04 for the RGB and 0.56 ± 0.09 for the MS in the TA. The uncertainties were derived from values of eccentricities created 1000 times by an MC method after incorporating the uncertainties in the distance, proper motions, and RV when calculating the eccentricity. In addition, we checked the scatter of the eccentricity uncertainties to ensure that the e-distribution for the RGB/MS sample is not an artifact generated by errors in the RV, distance, and proper motions. We obtained a dispersion of $0.06^{+0.06}_{-0.02}$ for the RGB and $0.08^{+0.03}_{-0.01}$ for the MS in the LA and $0.04^{+0.05}_{-0.01}$ for the RGB and $0.09^{+0.01}_{-0.01}$ for the MS in the TA. For the SC, which includes only RGB stars, the scatter is $0.08^{+0.01}_{-0.01}$. The errors were taken at 34% to the left and right of the median in each uncertainty distribution. We note the consistent behavior without large dispersions in the two different samples, although the MS sample is too small in each arm to compare to the RGB sample, as mentioned in Section 3.1. Nonetheless, this proves that the low-e population in the LA indeed exists. To our knowledge, this is the first time that a larger fraction of low-e stars is found in the LA compared with the TA and SC.

Similarly, panel (e) of Figure 2 exhibits the eccentricity distribution of the Sgr RR Lyrae stars. As noted in the RGB/MS sample, the TA and SC show a narrow distribution, with a peak of $e \sim 0.5$. In comparison, the LA exhibits a much broader e-distribution than that of our RGB/MS sample, ranging from 0.1 to 0.8 due to the larger distance coverage than the RGB/MS sample. Nonetheless, we clearly observe the low-e population ($e < 0.4$), confirming the existence of the low-e RGB/MS stars in the LA. The small eccentricity error and its small dispersion of $0.05^{+0.07}_{-0.01}$ for our RR Lyrae stars also support the presence of the low-e population.

Given that the stellar stream stripped off from a dwarf galaxy retains its progenitor's dynamical properties, such as eccentricity (Re Fiorentin et al. 2015; Amorisco 2017; Mackereth et al. 2019), one can expect that the LA, TA, and SC should have similar e-distributions. Thus, our result highlights an interesting new feature.

To further investigate the disparate e-distribution of the LA, we plot the metallicity profile of the Sgr members as a function of the stream longitude (Λ) for the RGB/MS sample in Figure 3. We excluded the RR Lyrae sample because there is no metallicity information for the SC stars. Note that the LA region is divided into A (metal-rich) and B (metal-poor) regions. The color code indicates the median eccentricity. The fraction of stars with $e < 0.4$ is listed in each region as well. Despite a relatively large scatter in each region, the figure clearly suggests that regions A and C have a relatively higher metallicity than region B; closer to the SC (large green circles), the metallicity becomes higher, implying some level of metallicity gradient along each region, as other recent studies

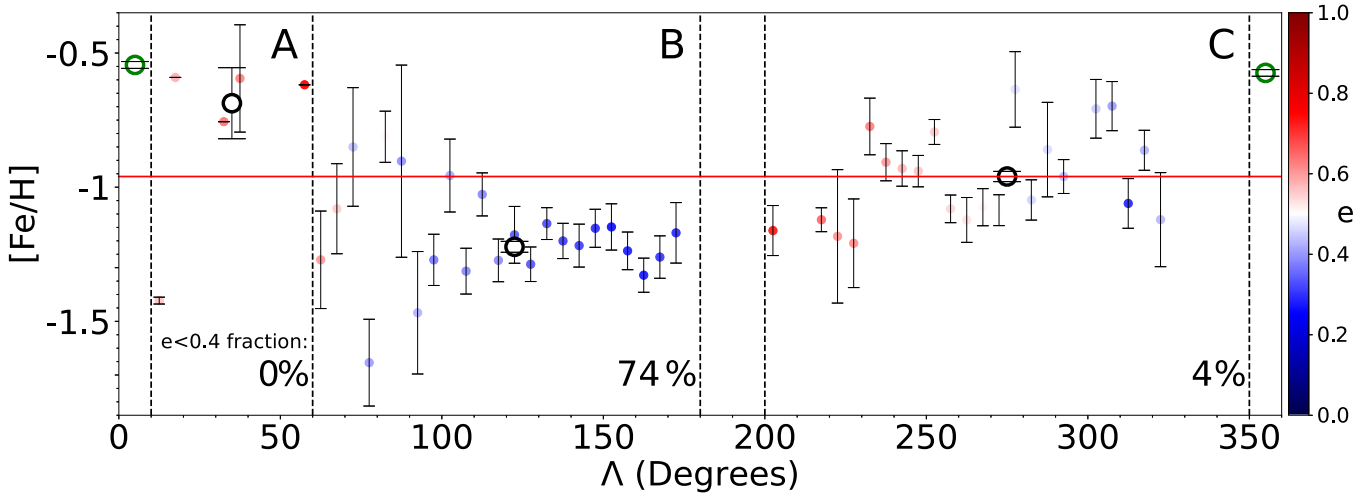

Figure 3. Metallicity profile of three regions (A, B, and C) as a function of Λ for the RGB/MS stars. Each point is a median value in a bin size of $\Lambda = 5°$; the error bar is the standard deviation. The color code represents the median eccentricity in each bin, and its scale is shown in the right color bar. The large open circles represent the median metallicity of the A, B, and C regions. Note that the LA is divided into two regions: metal-rich (A) and metal-poor (B). The red horizontal line indicates the median [Fe/H] of the TA. At the bottom of the figure, the fraction of stars with $e < 0.4$ in each region is listed.

have reported (e.g., Gibbons et al. 2017; Hayes et al. 2020; Ramos et al. 2022). We also observe that the low-e fraction for regions A and C is almost negligible, whereas region B has a large portion of stars with $e < 0.4$ (74%). Additionally, we clearly see from the color code that the low-e stars in the LA are dominated by relatively metal-poor stars located farther away from the SC. Taking the metallicity as a proxy for time, the older (metal-poor) population, which was stripped off first, possesses lower eccentricity. On the other hand, the TA stars exhibit an opposite trend; the (metal-poor) stars farther away from the SC exhibit higher eccentricity. These distinct features between the LA and TA stars unambiguously indicate a mixture of stars that have experienced different chemical and dynamical evolutionary histories.

4.3. Signature of Dynamical Evolution of Low-e Stars in the LA

We have found the e-distribution of the LA to be significantly different from that of the TA and SC (Figure 2), having a large fraction of low-e stars ($e < 0.4$) in our RGB/MS sample. These stars are both more metal-poor and located farther away from the SC, as seen in Figure 3. This dynamical dichotomy among the Sgr stream stars is also reported in at least one other study. Hasselquist et al. (2019) identified 35 Sgr member stars by applying a clustering algorithm to the APOGEE chemical abundances and found that 26 of these stars have eccentricities in the range of 0.40–0.85 and that nine likely Sgr members that belong to the LA exhibit relatively lower e (<0.4) than the Sgr main body. These characteristics qualitatively agree with our findings. However, they did not give much emphasis to these low-e stars. They also noted that the TA stars exhibit a range of $r_{\rm max} = 60$–120 kpc, while a range of $r_{\rm max} = 40$–60 kpc was found for the LA debris. Because one expects that a stellar stream stripped from a disrupted dwarf galaxy would follow similar dynamical characteristics (e.g., Johnston et al. 1996; van den Bosch et al. 1999; Re Fiorentin et al. 2015; Amorisco 2017; Mackereth et al. 2019), it is challenging to explain the contrasting e-behavior of the LA with respect to that of the TA and SC.

Then, where did the low-eccentricity stars in the LA come from? One might simply think that they are interlopers, perhaps from another dwarf galaxy that happened to be in the right place and have the right chemistry, similar to the LA of the Sgr stream. However, as a different possible progenitor associated with the low-e stars of the LA has not been identified, this assertion appears unlikely. It is more plausible to conjecture that the LA stars were stripped off in the early history of the Sgr disruption, as many simulations have suggested (Law & Majewski 2016; Ibata et al. 2020; Ramos et al. 2020; Vasiliev et al. 2021), and that they have been dynamically perturbed in such a way as to alter their orbits and become more circular than the TA and SC.

Using a catalog of the Sgr RGB stream members, V21 reported a clear misalignment between the Sgr stream track and the motion of the LA stars after correcting for the solar reflex motion in their observed proper motions, suggesting that the time-varying potential of the MW may perturb the Sgr's stream to alter its orbit. In fact, V21 carried out Sgr simulations that consider the perturbation of the MW caused by the LMC and found that, without the LMC, the Sgr stream stars would have larger apogalactic distances and higher eccentricity, indicating that the presence of the LMC causes the decrease of the initial eccentricity of the Sgr orbit. The LA is the most perturbed in their simulations. Consequently, the low-e stars we detected in the LA can be qualitatively explained by their prediction. It is important to recognize that the MW's reflex motion has a greater effect on the Sgr stream than for the LMC itself, given that the LA is located in the northern Galactic hemisphere, while the LMC is passing by in the southern hemisphere.

The above claim can be confirmed in panel (f) of Figure 2, which exhibits the e-distribution of the simulated Sgr stars perturbed by the MW interacting with the LMC. We grouped the model data into the LA, TA, and SC, same as in the RGB/MS sample. Even though the fraction is relatively smaller than that of the RGB/MS sample, we can identify the low-e population (<0.4). The reason that our RGB/MS stars have more low-e stars is the lack of RGB/MS stars in the LA region, which are close to the SC (see Figure 5). In fact, our RR Lyrae sample, which covers much larger distances and includes more stars close to the SC, exhibits a lower fraction of low-e stars in

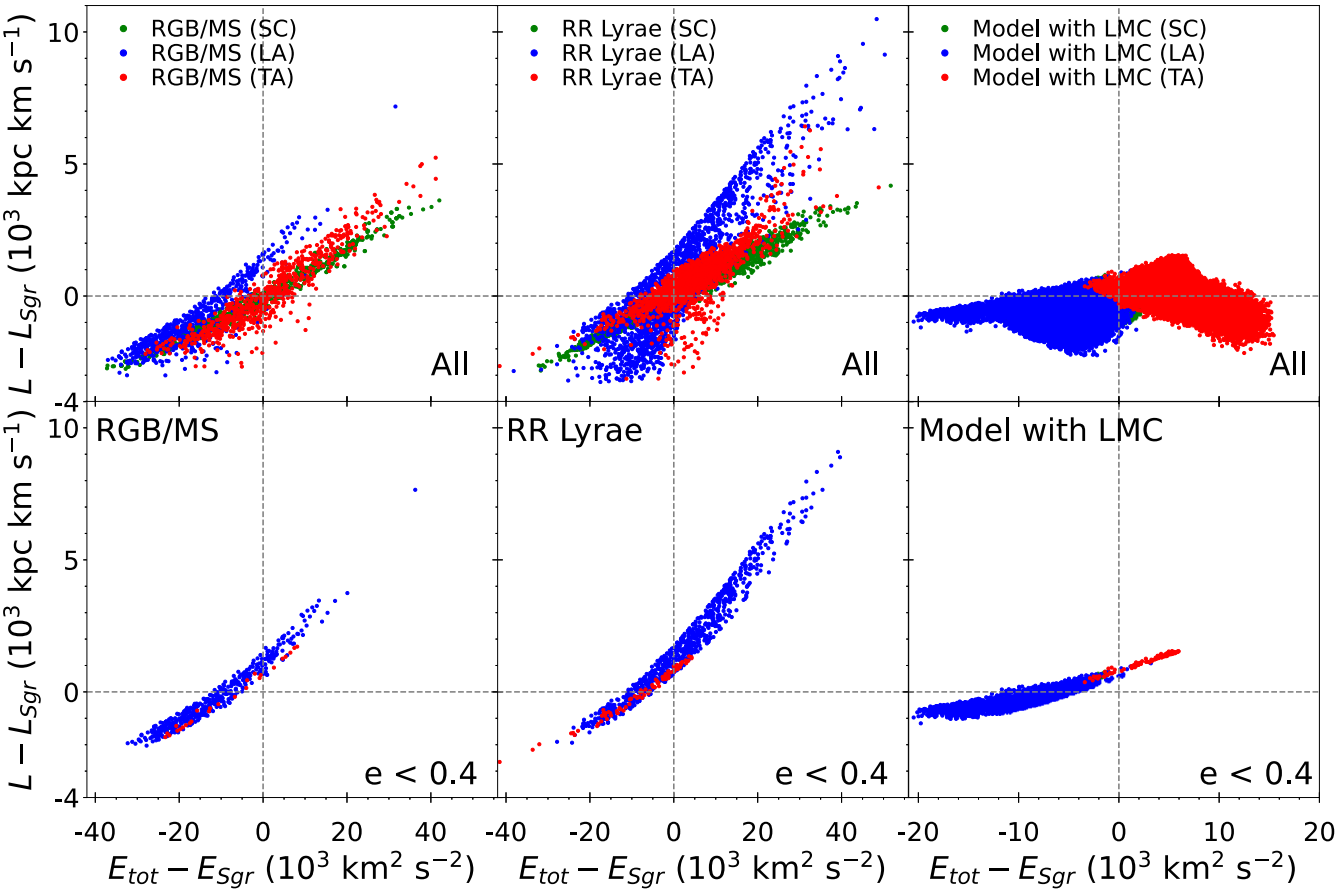

Figure 4. Angular momentum–energy (L–E) diagram for the RGB/MS stars (left panels), the RR Lyrae stars (middle panels), and a Sgr model with the LMC (right panels). The bottom panels are the stars with $e < 0.4$. Both the L and E quantities are rescaled to have zero at the location of the SC as in V21. The color code is the same as in Figure 2. Note that as the SC stars in the right panel are buried in the LA and TA, they are not clearly visible in the panel. We clearly see the offset of the LA from the TA and SC (top left), and we do not observe many stars with $e < 0.4$ in the TA and SC (bottom left). The RR Lyrae sample (bottom middle) exhibits the same pattern; qualitatively, a similar behavior is observed in the Sgr model with the LMC perturbation adopted from V21 (bottom right).

the LA (see panel (e) of Figure 2) than the RGB/MS sample, confirming our claim above.

The different behavior in the e-distribution should be reflected in the $r_{\rm max}$ distribution as well. Our RGB/MS sample has a mean $r_{\rm max}$ of 33.6 ± 0.6 kpc for the LA and 53.4 ± 1.0 kpc for the TA; thus, the LA has a shorter $r_{\rm max}$, as in other studies. However, we obtained a mean $r_{\rm max}$ of 33.9 ± 0.8 kpc for the low-e stars in the LA, unlike the expected shorter $r_{\rm max}$. As mentioned above, this is because the LA stars in our RGB/MS sample are dominated by the low-e stars that are farther away from the SC. However, the RR Lyrae stars, which contain more high-e stars close to the SC, yielded a mean $r_{\rm max}$ of 56.6 ± 0.3, 49.2 ± 0.4, and 47.1 ± 0.7 kpc for the TA, LA, and LA stars with $e < 0.4$, respectively, resulting in a smaller $r_{\rm max}$ for the low-e stars in the LA, as expected. The Sgr model with perturbation from the LMC has a more uniform stellar distribution and clearly suggests a shorter distance of $r_{\rm max}$; we derived a mean $r_{\rm max}$ distance of 45.3 and 37.6 kpc for the LA and the LA stars with $e < 0.4$, respectively. Therefore, we can interpret that the $r_{\rm max}$ distance of low-e stars in the LA became shorter due to the influence of the MW's reflex motion.

To investigate the connection of the low-e stars with the perturbation of the LMC more closely, we used the RGB/MS, RR Lyrae, and Sgr model samples to produce the angular momentum–energy (L–E) diagram in Figure 4, similar to Figure 11 of V21. The L and E quantities are rescaled to be zero at the SC in this figure. As V21 well illustrated, models of tidal tail formation (e.g., Helmi & de Zeeuw 2000; Eyre & Binney 2011; Gibbons et al. 2014) produce TAs and LAs that have distinct patterns in the L–E plane, in that they are shifted in opposite directions from their progenitor dwarf. That is, the trailing stars have higher energy and angular momentum, while the leading stars possess lower energy and angular momentum compared to their progenitor (see panel (d) of Figure 11 of V21). However, we do not observe this behavior in the top left panel of Figure 4; rather, the LA occupies a slightly higher angular momentum region than the SC at a given E, while the TA and SC overlap one another. This behavior is, to some degree, in line with the right panels of this figure, with no large offset seen in the angular momentum among the LA, TA, and SC, which was reproduced by adopting the model data of V21 that consider the time-dependent potential of the MW interacting with the LMC. Note that we recalculated L and E for each star using the Stäckel-type potential, as mentioned in Section 2.2. In the V21 simulations, the LMC perturbation is expected to cause the angular momentum (eccentricity) of the LA to increase (decrease) and the angular momentum (eccentricity) of the TA to decrease (increase).

The impact of the LMC perturbation is more clearly seen in the Sgr model data, which only show the stars with $e < 0.4$ (bottom right panel of Figure 4). It shows some fraction of stars with angular momentum differences larger than –1000 kpc km

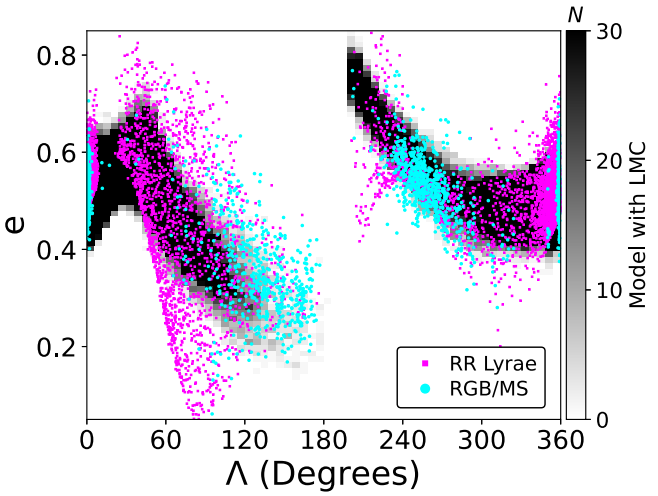

Figure 5. Eccentricity distribution as a function of Λ. The cyan dots are the RGB/MS stars, while the magenta points indicate the RR Lyrae stars. The black background represents the number density produced by a Sgr model with the LMC, which is adopted from V21. The cluster around $\Lambda \sim 0^\circ$ and 360° is the SC. We clearly observe that the eccentricity increases for the stars closer to the SC for the LA, while the opposite behavior is seen for the TA; the farthest stars from the SC have higher eccentricity.

s^{-1} in the LA, whereas the TA and SC stars are almost removed. Similarly, there is a lack of SC and TA stars in the RGB/MS sample (bottom left panel). Consequently, the top left panel of Figure 4 signals a significant evolution of the angular momentum of the LA after its stripping.

Our RR Lyrae sample also exhibits similar features, as seen in the middle panels of Figure 4, but thanks to the greater distance coverage and a larger sample size, we observe a larger fraction of stars with higher L and E stars than for the RGB/MS stars. As can be inferred from the bottom middle panel, the stars with a higher L than that of the SC sequence have low eccentricity. These low-e stars are located farther away from (closer to) the SC in the case of the LA (TA), as can be appreciated from inspection of Figure 5, which exhibits the eccentricity distribution as a function of Λ. Consequently, our findings provide additional evidence for the influence of the MW by the LMC on the dynamical evolution of the tidal debris of the Sgr stream, as envisaged by V21.

The fact that the TA is overlapped by the SC in the L–E plane suggests that the TA is also affected by the perturbation. According to the simulation by V21, the TA stars, which are located farther away from the SC, experience more angular momentum evolution due to disturbance by the LMC. As a result, they possess lower angular momentum and hence higher eccentricity. As evidence, we notice some fraction of high-e stars in the TA in panel (f) of Figure 2. Observationally, we can assess this behavior among the RR Lyrae stars (magenta) in Figure 5 as well. In this figure, the TA stars farther away from the SC ($200^\circ < \Lambda < 240^\circ$) have more eccentric orbits (e.g., lower angular momentum), in contrast to the LA stars ($\Lambda < 180^\circ$). The Sgr model (black background) with perturbation from the LMC confirms this pattern. These observational features clearly present that the stars close to the SC are less perturbed by the time-dependent potential of the MW by the LMC.

To conclude, our findings and interpretation confirm the dynamical evolution of the Sgr stream due to the reflex motion of the MW's center caused by the gravitational influence of the LMC. However, from a chemical perspective, one caveat of this dynamical interpretation, following the simulations of V21, is that if the LA and TA are simultaneously stripped off, it is difficult to reconcile the metallicity discrepancy between the LA and TA.

5. Conclusions

We have presented the chemical and dynamical properties of the Sgr member stars. The MDF of the LA is slightly shifted to a more metal-poor level than that of the TA. We obtained a mean value of $[Fe/H] = -1.14 \pm 0.12$ (sys) ± 0.03 (ran) for the LA and $[Fe/H] = -0.92 \pm 0.07$ (sys) ± 0.03 (ran) for the TA. The MDF of the SC is biased toward the more metal-rich region, yielding a mean of $[Fe/H] = -0.56 \pm 0.01$ (ran). We derived mean values of $[Mg/Fe] = +0.08 \pm 0.07$ (sys) ± 0.07 (ran), $+0.08 \pm 0.07$ (sys) ± 0.06 (ran), and -0.05 ± 0.02 (ran) for the LA, TA, and SC, respectively. These chemical features of the Sgr members agree well with recent studies (e.g., Hayes et al. 2020; Ramos et al. 2022; Limberg et al. 2023).

The chemical contrast among the LA, TA, and SC can be understood by a radial metallicity gradient due to different star formation histories in the progenitor of the Sgr dwarf. Because the old, metal-poor stars at the outer edge of the Sgr progenitor were preferentially stripped off, the stars in the LA, which were stripped first, are more metal-poor than the stars in the TA.

One striking finding in this study is the relatively larger fraction of low-e (<0.4) stars in the LA than in the TA and SC. As one can expect that a stellar stream stripped off from a dwarf galaxy closely follows the eccentricity of its progenitor, this behavior presents a challenge to understand. We attempted to explain the disparate e-distribution of the LA by appealing to time-dependent perturbations of the MW by the LMC, following the demonstration of V21. According to their simulations, the LA is perturbed the most, and the disturbance from the LMC to the Sgr tidal stream causes the decrease of eccentricity of the Sgr orbit, qualitatively in accordance with the eccentricity behavior seen in our LA stars.

The simulation by V21 also predicts that the TA stars, which are located farther away from the SC, experience more dynamical evolution due to disturbance from the LMC. We confirm this by finding high-e RR Lyrae stars in the TA region that are more distant from the SC.

Acknowledgments

We thank an anonymous referee for a careful review of this paper, which has improved the clarity of its presentation. This work was supported by Chungnam National University. T.C.B. acknowledges partial support for this work from grant PHY 14-30152, Physics Frontier Center/JINA Center for the Evolution of the Elements (JINA-CEE), awarded by the U.S. National Science Foundation, and from OISE-1927130: The International Research Network for Nuclear Astrophysics (IReNA), awarded by the U.S. National Science Foundation.

Funding for the Sloan Digital Sky Survey IV has been provided by the Alfred P. Sloan Foundation, the U.S. Department of Energy Office of Science, and the Participating Institutions.

The SDSS-IV acknowledges support and resources from the Center for High Performance Computing at the University of Utah. The SDSS website is www.sdss.org.

The SDSS-IV is managed by the Astrophysical Research Consortium for the Participating Institutions of the SDSS Collaboration, including the Brazilian Participation Group, the Carnegie Institution for Science, Carnegie Mellon University, Center for Astrophysics, Harvard & Smithsonian, the Chilean Participation Group, the French Participation Group, Instituto de Astrofísica de Canarias, The Johns Hopkins University, the Kavli Institute for the Physics and Mathematics of the Universe (IPMU)/University of Tokyo, the Korean Participation Group, Lawrence Berkeley National Laboratory, Leibniz Institut für Astrophysik Potsdam (AIP), Max-Planck-Institut für Astronomie (MPIA Heidelberg), Max-Planck-Institut für Astrophysik (MPA Garching), Max-Planck-Institut für Extraterrestrische Physik (MPE), National Astronomical Observatories of China, New Mexico State University, New York University, the University of Notre Dame, Observatário Nacional/MCTI, The Ohio State University, Pennsylvania State University, Shanghai Astronomical Observatory, the United Kingdom Participation Group, Universidad Nacional Autónoma de México, the University of Arizona, the University of Colorado Boulder, the University of Oxford, the University of Portsmouth, the University of Utah, the University of Virginia, the University of Washington, the University of Wisconsin, Vanderbilt University, and Yale University.

The Guoshoujing Telescope (the Large Sky Area Multi-Object Fiber Spectroscopic Telescope, LAMOST) is a National Major Scientific Project built by the Chinese Academy of Sciences, funded by the National Development and Reform Commission, and operated and managed by the National Astronomical Observatories, Chinese Academy of Sciences.

ORCID iDs

Gwibong Kang https://orcid.org/0009-0004-2765-1986
Young Sun Lee https://orcid.org/0000-0001-5297-4518
Young Kwang Kim https://orcid.org/0000-0002-6411-5857
Timothy C. Beers https://orcid.org/0000-0003-4573-6233

References

Abdurro'uf, Accetta, K., Aerts, C., et al. 2022, ApJS, 259, 35
Amorisco, N. C. 2017, MNRAS, 464, 2882
Beers, T. C., Carollo, D., Ivezić, Ž., et al. 2012, ApJ, 746, 34
Beers, T. C., Chiba, M., Yoshii, Y., et al. 2000, AJ, 119, 2866
Belokurov, V., Koposov, S. E., Evans, N. W., et al. 2014, MNRAS, 437, 116
Belokurov, V., Zucker, D. B., Evans, N. W., et al. 2006, ApJL, 642, L137
Bennett, M., & Bovy, J. 2019, MNRAS, 482, 1417
Bland-Hawthorn, J., & Gerhard, O. 2016, A&RAA, 54, 529
Bullock, J. S., & Johnston, K. V. 2005, ApJ, 635, 931
Carlin, J. L., Majewski, S. R., Casetti-Dinescu, D. I., et al. 2012, ApJ, 744, 25
Carlin, J. L., Sheffield, A. A., Cunha, K., et al. 2018, ApJL, 859, L10
Chambers, K. C., Magnier, E. A., Metcalfe, N., et al. 2016, arXiv:1612.05560
Chiba, M., & Beers, T. C. 2000, AJ, 119, 2843
Cooper, A. P., Cole, S., Frenk, C. S., et al. 2010, MNRAS, 406, 744
Eyre, A., & Binney, J. 2011, MNRAS, 413, 1852
Gaia Collaboration, Brown, A. G. A., Vallenari, A., et al. 2021, A&A, 649, A1
García Pérez, A. E., Allende Prieto, C., Holtzman, J. A., et al. 2016, AJ, 151, 144
Gibbons, S. L. J., Belokurov, V., & Evans, N. W. 2014, MNRAS, 445, 3788
Gibbons, S. L. J., Belokurov, V., & Evans, N. W. 2017, MNRAS, 464, 794
Hasselquist, S., Carlin, J. L., Holtzman, J. A., et al. 2019, ApJ, 872, 58
Hayes, C. R., Majewski, S. R., Hasselquist, S., et al. 2020, ApJ, 889, 63
Helmi, A., & de Zeeuw, P. T. 2000, MNRAS, 319, 657
Hernitschek, N., Sesar, B., Rix, H.-W., et al. 2017, ApJ, 850, 96
Ibata, R., Bellazzini, M., Thomas, G., et al. 2020, ApJL, 891, L19
Ibata, R., Irwin, M., Lewis, G. F., et al. 2001, ApJL, 547, L133
Ibata, R. A., Gilmore, G., & Irwin, M. J. 1994, Natur, 370, 194
Johnson, B. D., Conroy, C., Naidu, R. P., et al. 2020, ApJ, 900, 103
Johnston, K. V., Hernquist, L., & Bolte, M. 1996, ApJ, 465, 278
Jönsson, H., Holtzman, J. A., Allende Prieto, C., et al. 2020, AJ, 160, 120
Kawata, D., Bovy, J., Matsunaga, N., et al. 2019, MNRAS, 482, 40
Kim, C., Lee, Y. S., Beers, T. C., & Kim, Y. K. 2023, JKAS, 956, 59
Kim, Y. K., Lee, Y. S., & Beers, T. C. 2019, ApJ, 882, 176
Kim, Y. K., Lee, Y. S., Beers, T. C., et al. 2021, ApJL, 911, L21
Koposov, S. E., Belokurov, V., Evans, N. W., et al. 2012, ApJ, 750, 80
Law, D. R., & Majewski, S. R. 2010, ApJ, 718, 1128
Law, D. R., & Majewski, S. R. 2016, in Tidal Streams in the Local Group and Beyond, ed. H. Newberg & J. Carlin, Vol. 420 (Cham: Springer), 31
Lee, A., Lee, Y. S., Kim, Y. K., Beers, T. C., & An, D. 2023, ApJ, 945, 56
Lee, Y. S., Beers, T. C., Allende Prieto, C., et al. 2011, AJ, 141, 90
Lee, Y. S., Beers, T. C., Carlin, J. L., et al. 2015, AJ, 150, 187
Lee, Y. S., Beers, T. C., & Kim, Y. K. 2019, ApJ, 885, 102
Lee, Y. S., Beers, T. C., Sivarani, T., et al. 2008a, AJ, 136, 2022
Lee, Y. S., Beers, T. C., Sivarani, T., et al. 2008b, AJ, 136, 2050
Leung, H. W., & Bovy, J. 2019, MNRAS, 489, 2079
Li, C., Xue, X., Zhong, J., et al. 2019, ApJ, 874, 138
Limberg, G., Queiroz, A. B. A., Perottoni, H. D., et al. 2023, ApJ, 946, 66
Lindegren, L., Klioner, S. A., Hernández, J., et al. 2021, A&A, 649, A2
Luo, A.-L., Zhao, Y.-H., Zhao, G., et al. 2019, yCat, 5164, 0
Mackereth, J. T., Schiavon, R. P., Pfeffer, J., et al. 2019, MNRAS, 482, 3426
Majewski, S. R., Skrutskie, M. F., Weinberg, M. D., et al. 2003, ApJ, 599, 1082
Naidu, R. P., Conroy, C., Bonaca, A., et al. 2020, ApJ, 901, 48
Newberg, H. J., Yanny, B., Rockosi, C., et al. 2002, ApJ, 569, 245
Ramos, P., Antoja, T., Yuan, Z., et al. 2022, A&A, 666, A64
Ramos, P., Mateu, C., Antoja, T., et al. 2020, A&A, 640, C5
Re Fiorentin, P., Lattanzi, M. G., Spagna, A., et al. 2015, AJ, 150, 128
Rockosi, C. M., Lee, Y. S., Morrison, H. L., et al. 2022, ApJS, 259, 60
Schönrich, R., Binney, J., & Dehnen, W. 2010, MNRAS, 403, 1829
van den Bosch, F. C., Lewis, G. F., Lake, G., et al. 1999, ApJ, 515, 50
Vasiliev, E., Belokurov, V., & Erkal, D. 2021, MNRAS, 501, 2279
Wang, J., Shi, J., Zhao, Y., et al. 2016, MNRAS, 456, 672
Xiang, M., Ting, Y.-S., Rix, H.-W., et al. 2019, ApJS, 245, 34
Yanny, B., Newberg, H. J., Kent, S., et al. 2000, ApJ, 540, 825
Yanny, B., Rockosi, C., Newberg, H. J., et al. 2009, AJ, 137, 4377
York, D. G., Adelman, J., Anderson, J. E., et al. 2000, AJ, 120, 1579